**International Journal of Minerals, Metallurgy and Materials**
**Accepted manuscript, https://doi.org/10.1007/s12613-024-3085-3**


# Influence of unloading orifice size on the production of micro-sized ore particle production by gas rapid unloading

*Genghao Zhang*[1)], *Deyang zhao*[1)], *Chang Yi*[2)], *Yongbo Fan*[3),✉], *Renshu Yang*[1),✉], *and Shihai Li*[3)]

1) School of Civil and Resource Engineering, University of Science and Technology Beijing, Beijing 100083, China

2) School of Reliability and Systems Engineering, Beihang University, Beijing 100191, China

3) Key Laboratory for Mechanics in Fluid Solid Coupling Systems, Institute of Mechanics, Chinese Academy of Sciences, Beijing 100190 China

Corresponding authors: Fan Yongbo E-mail: ybfan@imech.ac.cn; Yang Renshu E-mail: rsyem123@163.com

**Abstract:** Gas rapid unloading (GRU) is an innovative technology for ore comminution. Increasing the production of fine powder in each ore grinding cycle is vital for scaling up the GRU method to industrial applications. This study utilizes lab experiments to demonstrate that moderately reducing the orifice size significantly enhances pulverization and increases fine particle yield. Numerical simulations suggest that smaller orifices improve pulverization by increasing jet speed, reducing pressure drop, and creating a larger pressure difference inside and outside the unloading orifice. The orifice size should be optimized based on feed size to ensure efficient ore discharge. Reducing the unloading orifice size improves GRU grinding efficiency and energy use, offering guidance for the design of ore discharge ports in future industrial-scale equipment.

**Keywords：** iron ore pulverization, high-pressure gas, rapid unloading, orifice size, high-pressure gas jets

## 1. Introduction

Mineral resources are fundamental to modern human society[1, 2]. Ore comminution stands at the upstream of current industrial system. Most ores, except coastal sand mines, must undergo comminution before subsequent sorting and

industrial applications[3, 4]. Since the 2016 Paris Agreement, with over 113 countries committed, energy conservation and emission reduction have become global imperatives[5, 6]. Thus, ore grinding faces new opportunities and challenges in meeting current economic and environmental needs. Over the past 40 years, significant developments in traditional mechanical grinding technology can be summarized as equipment scaling, the introduction of new materials, the development of new equipment, and the application of intelligent control[7-9]. However, ore comminution remains an energy-intensive process, consuming up to 4% of global electrical energy[10-12]. The predominant method for ore comminution involves multi-stage crushing and ball milling[13-18]. Although ball mills offer advantages such as high processing capacity and continuous production, their energy conversion efficiency typically ranges from 1% to 2%[19, 20]. High-Pressure Grinding Rolls (HPGR) are a notable innovation in mechanical grinding, offering high efficiency, energy savings, and significant improvements in mineral liberation[21, 22]. However, the inherent boundary effects during grinding have not been fully resolved. Stirred mills such as Vertimill® and IsaMill offer significant advantages in fine grinding by providing better mixing of grinding media, with energy consumption 30% to 50% lower[23-27]. As a result, stirred mills show a significant cost advantage in fine grinding applications and could gradually replace ball mills in coarse particle grinding. Meanwhile, non-mechanical methods, such as high-voltage pulses[28-30], high-pressure water jets[31, 32], radio-frequency technology[33] and microwave pre-treatment[34], offer promising alternatives but remain limited in scalability and industrial application.

Gas Rapid Unloading (GRU) is an innovative non-mechanical ore comminution method. The GRU technique involves injecting high-pressure gas into the ore and rapidly decompressing it to induce tensile failure, pulverizing the ore into micrometer-sized particles within milliseconds[35, 36]. Studies have confirmed the feasibility and versatility of GRU for ore comminution[37, 38]. Compared to traditional grinding methods, GRU achieves rapid pulverization with a single gas unloading cycle in milliseconds, eliminating multiple grinding stages and reducing

processing time. Ore, with high compressive strength but low tensile resistance, requires about one-tenth the energy for tensile failure compared to compressive failure[39, 40]. GRU utilizes high-pressure gas decompression to induce ore tensile failure from within, theoretically consuming less energy. The grinding mechanism of the GRU method and other comminution machines is shown in Table 1. Meanwhile, GRU utilizes gas as the working medium, eliminating the need for grinding media like steel balls and minimizing material wear. Additionally, GRU shows consistent performance across different ore sizes without significant size effects, indicating substantial potential for industrial production[41]. However, GRU technology is still in the early stages of development and is not yet ready for full industrial application. Moreover, GRU requires the infiltration chamber to be fully released before feeding and proceeding to the next cycle. Therefore, practical applications require multiple chambers linked in a system to achieve continuous feeding and discharging. Additionally, the high-speed gas release in each cycle generates impact loads on the equipment, making long-term reliability a critical challenge for its commercialization.

The limitation of GRU in producing fine powder within a single grinding cycle also presents challenges in meeting the requirements for subsequent sorting processes. Modifying the unloading orifice size to change the flow field during rapid gas discharge may enhance fine particle production. This study examined the effect of unloading orifice size on the efficiency of the GRU method. Laboratory results show that smaller orifices increase fine particle yield and reduce overall particle size. Simulations indicate that smaller orifices increase gas jet velocity and pressure gradients, enhancing pulverization efficiency. These insights support the industrialization of the GRU method and guide future equipment design.



**Table 1. The grinding mechanism of different comminution machine**

| | |
|---|---|
| Destruction Mechanism | 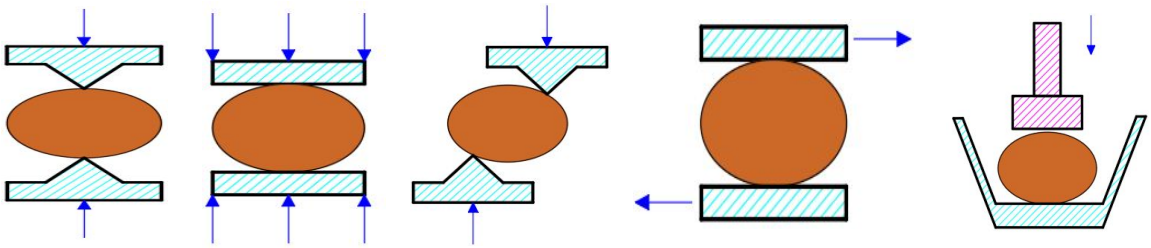 |

| | a. Split | b. Crush | c. Bend | d. Grinding | e. Impact |
|---|---|---|---|---|---|
| Jaw crusher | √ | √ | √ | × | × |
| Cone crusher | × | √ | √ | × | × |
| Ball Mill | × | √ | × | √ | √ |
| Jet mill | × | √ | × | √ | √ |
| HPGR | √ | √ | × | √ | × |

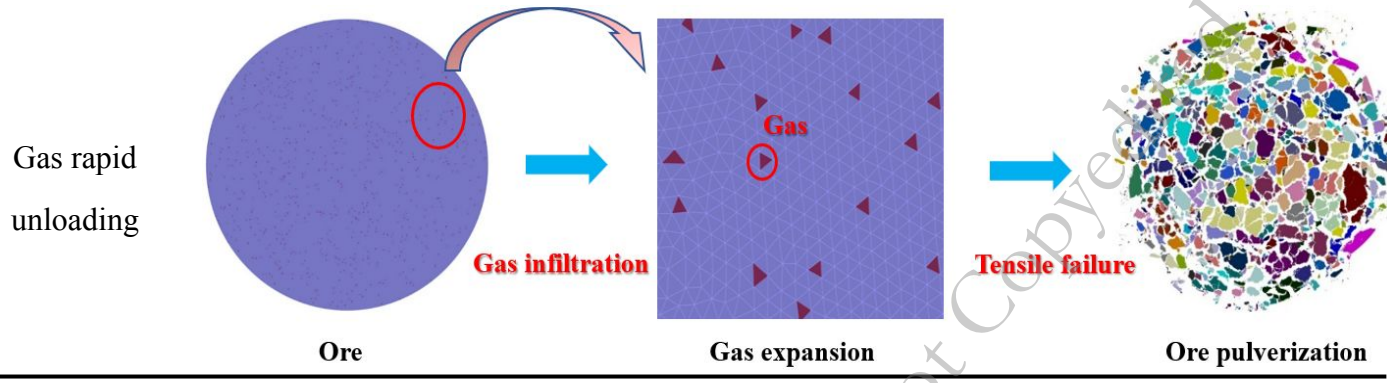


## 2. Methodology

### 2.1 Experiment method

The experimental setup for the GRU method includes two configurations. The first is a rear-mounted explosive design (Fig. 1), where the explosive is placed at the back of the high-pressure infiltration chamber. During the experiment, detonating the explosive generates high temperatures and pressures, quickly raising the gas pressure inside the infiltration chamber and causing the rupture disc to break instantly. At the same time, the explosive gases propel the ore within the chamber. When the rupture disc opens, the ore is rapidly expelled from the high-pressure infiltration chamber into the collection chamber. The second configuration uses an optimized design with a front-mounted explosive and high-pressure gas propulsion (Fig. 2). In this setup, the explosive primarily serves to open the rupture disc instantaneously, exerting minimal direct influence on ore pulverization. A propulsion chamber at the rear of the high-pressure infiltration chamber replaces the explosive to push the ore forward. This design allows for a more detailed analysis of pressure effects on ore pulverization, offering valuable insights for developing industrial-scale continuous production systems.

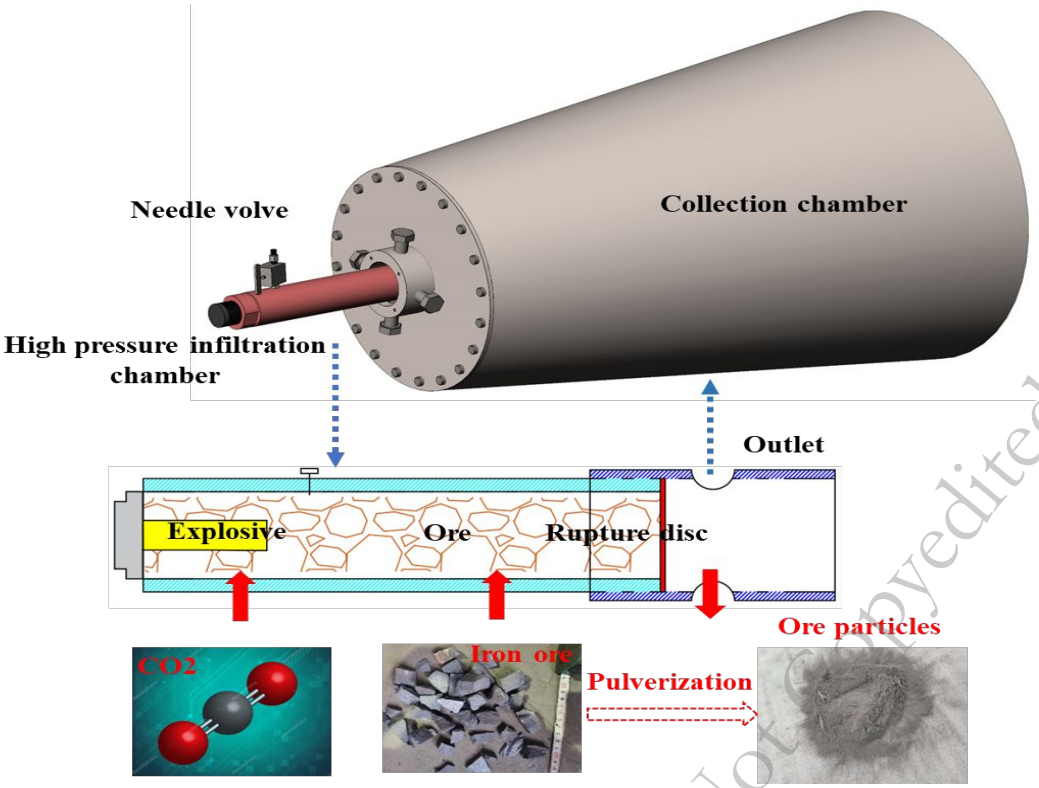


**Fig . 1. | The Schematic diagram of the rear-mounted explosive experiment apparatus**

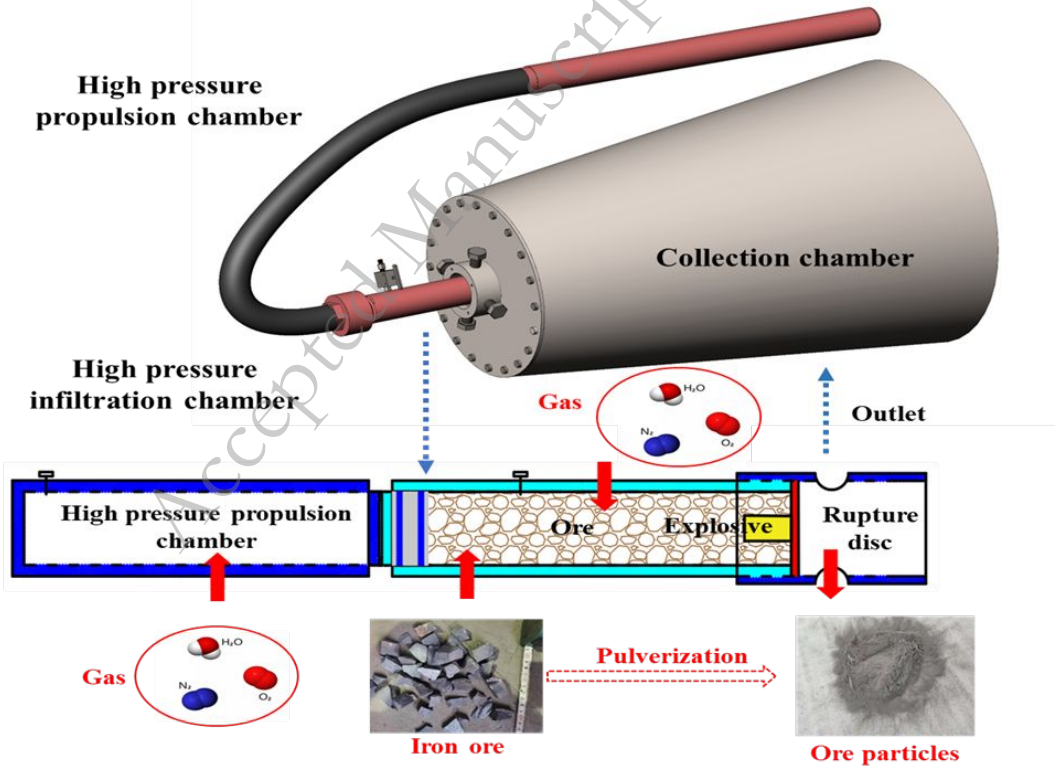


**Fig. 2. | The Schematic diagram of the front-mounted explosive experiment apparatus**

The GRU experiment for ore pulverization includes four main stages: (1) Placing

the ore inside the high-pressure infiltration chamber and assembling the apparatus. (2) Injecting high-pressure gas into the infiltration chamber, and in the second configuration, also into the propulsion chamber, allowing the working gas (or fluid) to permeate the ore's micro-pores. (3) Detonating the explosive to quickly open the rupture disc and initiate ore pulverization. (4) Opening the collection chamber to retrieve the pulverized ore.

To systematically investigate the effect of unloading orifice size on GRU effectiveness in ore pulverization, we first utilized carbon dioxide as the working fluid in a rear-mounted explosive setup to pulverize Longxin (LX) iron ore. Next, we employed the front-mounted explosive setup combined with high-pressure propulsion, using air as the working fluid, to pulverize Baogang (BG) iron ore.

We installed a circular ring between the discharge head and the rupture disc to adjust the unloading orifice size. Upon detonation, the pressure inside the infiltration chamber rapidly increases, severing the edge where the rupture disc overlaps with the circular ring's center hole. During the gas rapid unloading process, the ore is expelled through the center hole along with the gas jet. By varying the diameter of the circular ring's center hole, the unloading orifice size can be precisely controlled. The installation process of the circular ring and a schematic diagram of the experimental setup are illustrated in Fig. 3.

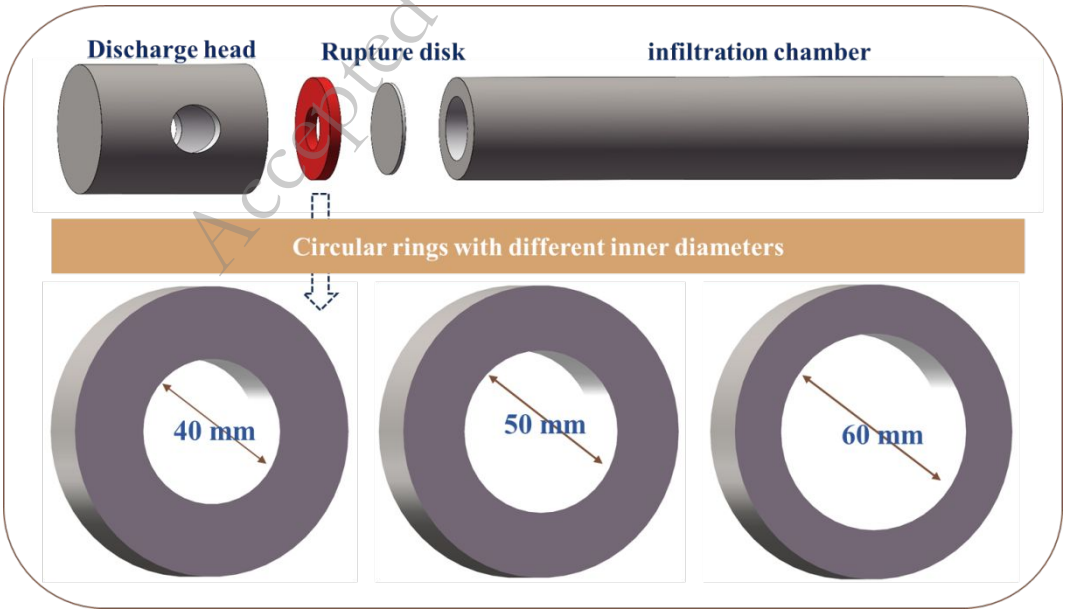


**Fig. 3. | The installation method of the circular ring and the schematic of**

**experiment equipment**

## 2.2 Experimental materials

The experiment taken LX iron ore and BG iron ore as the experimental materials. First, we examined the mechanical properties of LX and BG iron ores, including uniaxial compressive strength, uniaxial tensile strength, porosity, and permeability. The materials and devices used to test physical and mechanical properties are shown in Fig. 4.

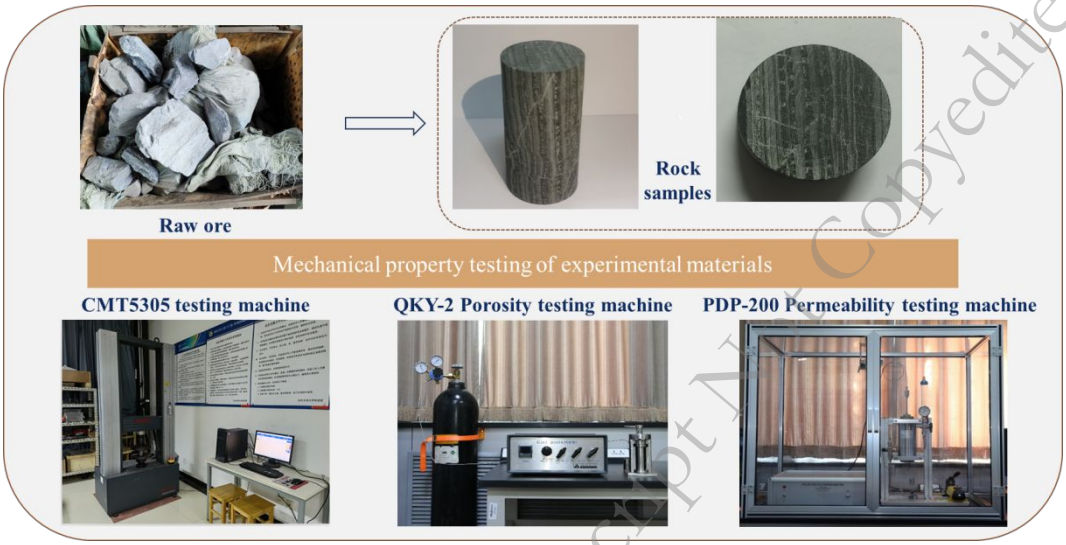


**Fig. 4. | Materials and devices for testing physical and mechanical properties**

The average uniaxial compressive strengths of LX and BG are 25.7 MPa and 55.45 MPa, respectively. The average uniaxial tensile strengths of LX and BG are 2.68 MPa and 8.4 MPa, respectively. Additional mechanical parameters of LX and BG iron ores are provided in Table 2.

**Table 2. The physical and mechanical parameters of the experimental materials**

| | Uniaxial Compressive Strength (MPa) | Uniaxial Tensile Strength (MPa) | Porosity (%) | Permeability (nD) |
|---|---|---|---|---|
| LX1 | 20 | 2.57 | 0.3026 | 1.117 |
| LX2 | 35 | 3.27 | - | - |
| LX3 | 22 | 2.19 | - | - |
| Average value | 25.7 | 2.68 | 0.3026 | 1.117 |

| | | | | |
|---|---|---|---|---|
| BG1 | 58.04 | 7.75 | 0.6237 | 16.539 |
| BG2 | 52.14 | 9.2 | - | - |
| BG3 | 56.17 | 8.26 | - | - |
| Average value | 55.45 | 8.4 | 0.6237 | 16.539 |

**2.3 Experimental Conduct**

We conducted pulverization experiments on LX iron ore using the rear-mounted explosive apparatus. To control the unloading orifice size, circular rings with a thickness of 10 mm, an outer diameter of 85 mm and inner diameters of 40 mm, 50 mm, and 60 mm were installed at the front end of the infiltration chamber. Each group of ore weighed 900 g, with a size of 2 to 3 cm. The detailed experimental parameters for LX iron ore are shown in Table 3.

**Table 3. Experimental Parameters for LX iron ore**

| | Ring inner diameter (mm) | Working Fluid | Infiltration Pressure (MPa) | Thickness of rupture disc (mm) | Ore weight (g) |
|---|---|---|---|---|---|
| LX 1 | 60 | $CO_2$ | 6 | 3 | 900 |
| LX 2 | 50 | $CO_2$ | 6 | 3 | 900 |
| LX 3 | 40 | $CO_2$ | 6 | 3 | 900 |

The experimental procedure began by placing the LX iron ore into the infiltration chamber, installing a circular ring between the discharge head and the rupture disc, and assembling the experimental apparatus. High-pressure liquid $CO_2$ was injected into the chamber, and the explosive was detonated to complete the experiment. The procedure for pulverizing BG iron ore was similar to that for LX iron ore, but it involved injecting 8 MPa and 12 MPa high-pressure air into the high-pressure infiltration chamber and propulsion chamber, respectively. In the front-mounted

explosive setup, the propulsion chamber replaces the explosive's propelling effect on the ore. The higher propulsion pressure expels the ore from the infiltration chamber at high velocity, creating a high-pressure gradient that facilitates effective pulverization of the ore. Detailed experimental parameters for BG iron ore are provided in Table 4.

**Table 4. Experimental Parameters for BG iron ore**

| | Ring inner diameter (mm) | Working Gas | Infiltration Pressure (MPa) | Propulsion Pressure (MPa) | Thickness of rupture disc(mm) | Ore weight (g) |
|---|---|---|---|---|---|---|
| BG 1 | 60 | Air | 8 | 12 | 3 | 1500 |
| BG 2 | 50 | Air | 8 | 12 | 3 | 1500 |
| BG 3 | 40 | Air | 8 | 12 | 3 | 1500 |

After the experiment, the pulverized products were extracted from the collection chamber and sieved for analysis. The Fig. 5 compares LX and BG iron ores before and after pulverization. The Fig. 6 illustrates the rupture disc destruction under different circular ring diameters.

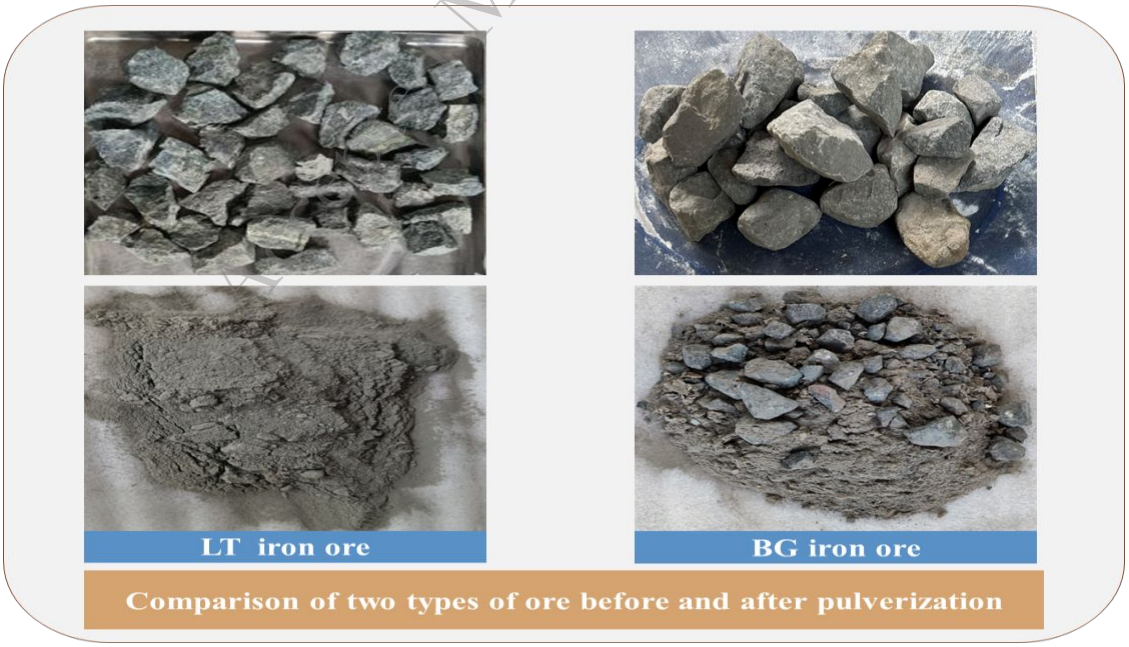


**Fig. 5. | The comparison of two types of iron ores before and after pulverization**

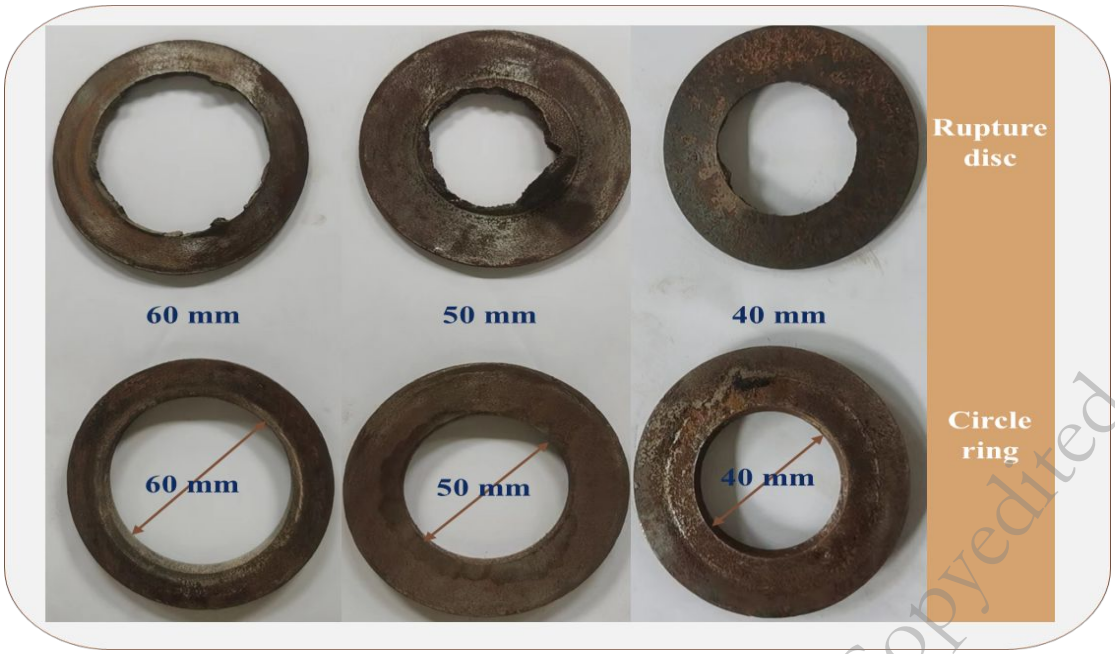


**Fig. 6. | The destruction of rupture discs under different diameter circular ring conditions.**

## 3. Result

### 3.1 Correlation analysis of the unloading orifice size and the particle size distribution of Longxin iron ore pulverization products

After the experiment, the pulverized LX iron ore was selected and the particle size distribution (PSD) is presented in Fig 7a. The results indicate that reducing the unloading orifice size significantly enhances the pulverization of LX iron ore. Specifically, reducing the unloading orifice size from 60 mm to 50 mm decreases the proportion of particles larger than 4 mm by about 14%, while the proportion of -0.5 mm particles only increases by around 3%. A further reduction in the orifice size to 40 mm results in a notable improvement in pulverization, with the total output of -0.5 mm LX iron ore powder reaching 80%. Compared to the 50 mm orifice, the increase in fine-grained pulverization products is mainly concentrated in the -74 μm range, with nearly a 15% rise in the proportion of -45 μm particles, and the output of +45 to -74 μm powder increases by about 7%. Correspondingly, the output of coarse particles (+0.5 mm) significantly decreases when the unloading orifice size is reduced to 40 mm. The output of +0.5 to 4 mm particles decreases by 10% and 7% compared to the 50 mm and 60 mm orifice sizes, respectively, while the output of +4 mm

particles decreases by 11% and 25%.

We further employed the Rosin-Rammler (R-R) function to characterize the overall cumulative PSD of pulverized products obtained from different unloading orifice sizes[42-44]. The general form of the R-R function is given in Equation 1.

$$F(x) = 1 - \exp[-(\frac{x}{X_0})^n] \quad \textbf{(1)}$$

where $x$ is the particle size (mm), $X_0$ is the particle size with a cumulative rate under sieve of 63.1%, representing the average particle size, $n$ is the non-uniformity index representing the degree of non-uniformity of the particle distribution.

The R-R function accurately fits the PSD of the pulverized LX iron ore products. The goodness-of-fit ($R^2$) values consistently exceed 0.98. Detailed fitting results are shown in Table 5. The fitting results exhibit as the unloading orifice size decreases, the average particle size $X_0$ of the LX pulverized products decreases from 1.8 mm to 0.163 mm, while the non-uniformity index fluctuates within a narrow range.

**Table 5. Fitting results**

| Opening Size | Characteristic Size $X_0$ | Uniformity Constant | $R^2$ |
|---|---|---|---|
| 4 cm | 0.163 mm | 0.40869 | 0.98 |
| 5 cm | 0.717 mm | 0.42437 | 0.99 |
| 6 cm | 1.80 mm | 0.37797 | 0.98 |

Fig. 7b shows the changes in cumulative PSD, average particle size, and uniformity index of pulverized LX iron ore under different unloading orifice sizes. The results indicate that an appropriate reduction in unloading orifice size can significantly improve the effectiveness of the rear-detonation GRU method for ore pulverization.

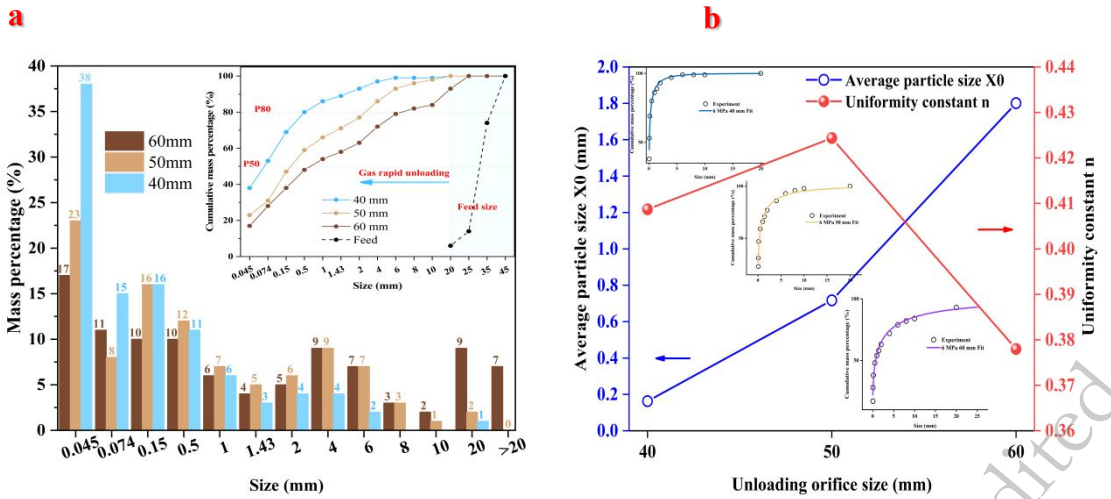


**Fig. 7.** | The characteristics of PSD of pulverized LX iron ore obtained at different unloading orifice sizes. **a.** The PSD of pulverized LX iron ore obtained at different unloading orifice sizes. **b.** The average particle size $X_0$ and non-uniformity coefficient of pulverized LX iron ore at different unloading orifice sizes.

### 3.2 Correlation analysis of the unloading orifice size and the particle size distribution of Baogang iron ore pulverization product

#### 3.2.1 Ore blockage due to undersized unloading orifice

We conducted pulverization experiments on BG iron ore using front-mounted explosive setups. The unloading orifice sizes were set to 60 mm, 50 mm, and 40 mm. Reducing the orifice size to 40 mm caused significant ore blockage (Fig. 8). A similar phenomenon occasionally occurs with rear-mounted explosive setups, but at a much lower frequency. This is due to the greater pushing force generated by rear-mounted explosives compared to the gas propulsion in front-mounted configurations. Thus, smaller unloading orifice sizes are more likely to cause ore blockage in front-mounted setups.


**Fig. 8. Ore Blockage at the 40 mm Unloading Orifice.**

Experimental data show that with a 40 mm unloading orifice, only 20% of the ore is ejected, while most remains in the infiltration chamber. Sieving analysis indicates that the retained ore undergoes minimal pulverization, primarily due to compression from the rear gas chamber. The PSD of BG iron ore retained in the infiltration chamber is shown in Table 7. Particles smaller than 0.5 mm make up just 5% of the total ore mass inside the chamber. These findings emphasize the critical role of high-speed gas unloading in effective ore pulverization and the need to optimize the unloading orifice size based on feed size.

### 3.2.2 Particle Size Distribution of Pulverized BG Iron Ore under Different Unloading Orifice Sizes

At an unloading orifice size of 60 mm, the GRU method for pulverizing BG iron ore produces 9% of particles at -45 μm, 17% at -74 μm, and 37% at -0.5 mm. While reducing the orifice size to 50 mm does not significantly increase the fraction of -0.5 mm particles, the proportion of coarse particles is substantially diminished. Specifically, the fraction of particles larger than 20 mm drops to 5%, a decrease of 12% compared to the 60 mm orifice. Further reducing the orifice size to 40 mm significantly enhances pulverization efficiency in the ejected ore, resulting in 24% of particles at -45 μm, 63% at -74 μm, and 77% at -0.5 mm, with a maximum particle size of less than 8 mm. In contrast, the pulverization of ore retained within the chamber remains limited, with only about 5% of particles at -0.5 mm and more than 40% of particles exceeding 20 mm. Most of the ore undergoes fracturing primarily due to compressive and impact forces, resulting in particles mainly within the +0.5

mm to 20 mm range. The PSD of BG iron ore pulverized at different unloading orifice sizes is shown in Fig 9a.

We further fitted the overall PSD of pulverized BG iron ore under three unloading orifice sizes using the R-R function. The fitting results presented in Table 6. The goodness-of-fit ($R^2$) values are consistently above 0.98, demonstrating that the R-R function accurately models the cumulative PSD of pulverized BG iron ore across different unloading orifice sizes. The fitting results show a trend of decreasing particle size with smaller unloading orifice sizes. As the orifice size decreases from 60 mm to 40 mm, the average particle size of the pulverized product decreases from 5.1 mm to 0.09 mm. Fig. 9b illustrates the changes in PSD, average particle size, and uniformity coefficient of pulverized BG iron ore under different unloading orifice sizes.

**Table 6. Fitting results**

| Opening Size | Characteristic Size | Uniformity Constant | $R^2$ |
|---|---|---|---|
| 40 mm | 0.09 | 0.260 | 0.99 |
| 50 mm | 4.29 | 0.455 | 0.98 |
| 60 mm | 5.1 | 0.376 | 0.98 |

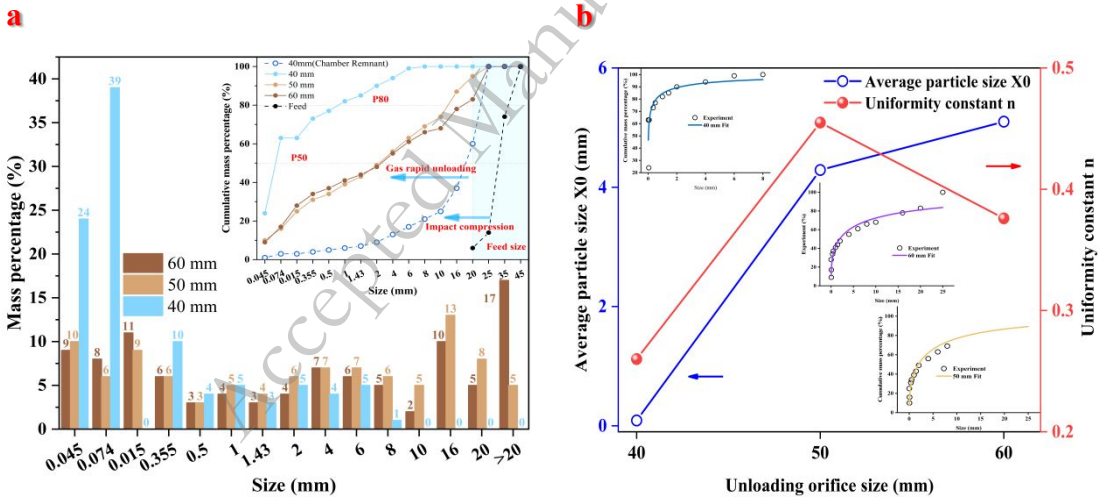


**Fig. 9.** | The characteristics of PSD of pulverized BG iron ore obtained at different unloading orifice sizes. **a.** The PSD of pulverized BG iron ore obtained at different unloading orifice sizes. **b.** The average particle size $X_0$ and non-uniformity coefficient of pulverized BG iron ore at different unloading orifice sizes.

## 4. Discussion

### 4.1. Discussion about the mechanism of reducing unloading orifice size facilitates ore pulverization

Changing the unloading orifice size affects the spatiotemporal evolution of the gas rapid unloading flow field. The velocity and pressure variations during the gas rapid unloading process with different unloading orifice sizes were analyzed in detail using Fluent. The computational model is shown in Fig. 10a, where the left region represents the interior of the high-pressure infiltration chamber, and the right region represents the atmospheric environment. The model is divided into 118,926 square grids, each with a side length of 3 mm.

Monitoring points P1, P2, and P3 are arranged from left to right along the axis direction: 5 mm from the outlet of the infiltration chamber, at the right center of the circular ring, and 5 mm from the outlet of the circular ring. The variation of jet velocity and pressure over time at these three points is monitored. Details of the computational model, locations of the monitoring points, and monitoring information are illustrated in Fig. 10b.

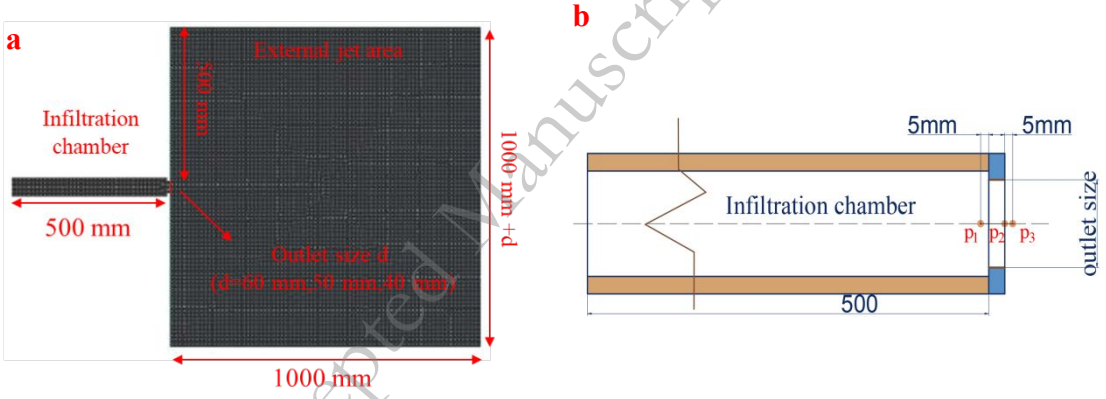


**Fig. 10.** | The caiculation model of carbon dioxide jet under different unloading orifice sizes. **a.** Calculate the geometric information of the model. **b.** The monitoring points locations of the model

Numerical simulations are conducted using $CO_2$ as the working fluid, modeled as an ideal gas. The initial pressure of $CO_2$ is set to 50 MPa, with detailed computational parameters provided in Table 7. Following the detonation of the explosive, the liquid $CO_2$ in the high-pressure chamber transitions to a high-pressure gaseous state.

Therefore, the simulations focus exclusively on the rapid unloading process of gaseous $CO_2$.

**Table 7. The Computational Model of CFD**

| Viscous Model | Gas Model | Multiphase Flow Model | Solver Model |
|---|---|---|---|
| K-omega (2 eqn)/SST | Ideal-gas | Mixture | PISO |

In the simulations, we monitored the temporal evolution of velocity and pressure at three key points: P1, P2, and P3. The pressure-time curve at P1 represents the internal pressure of the infiltration chamber over time. The velocity at P2 is used to determine the jet velocity of $CO_2$, while the pressure difference between P3 and P1 defines the pressure gradient across the unloading orifice. Fig. 11 shows the time-dependent profiles of $CO_2$ jet velocity, internal chamber pressure, and pressure gradient for different unloading orifice sizes.

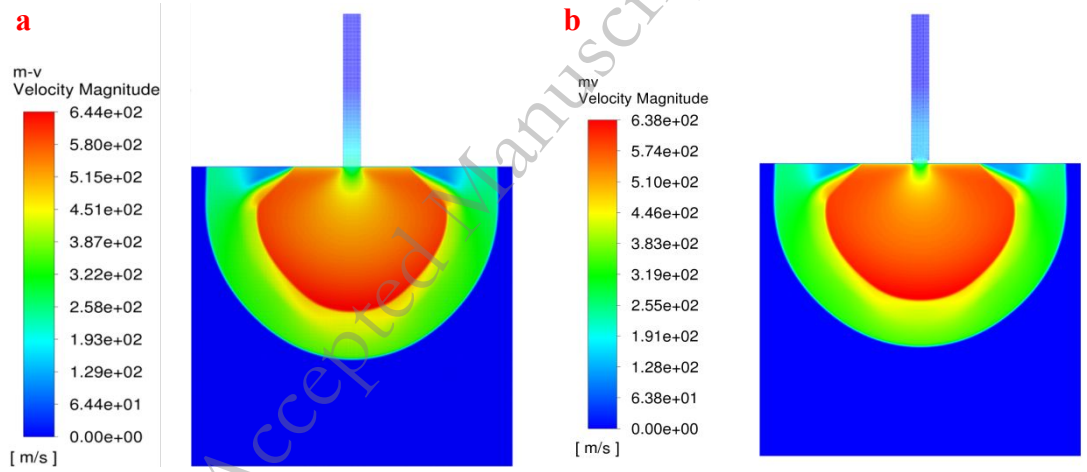

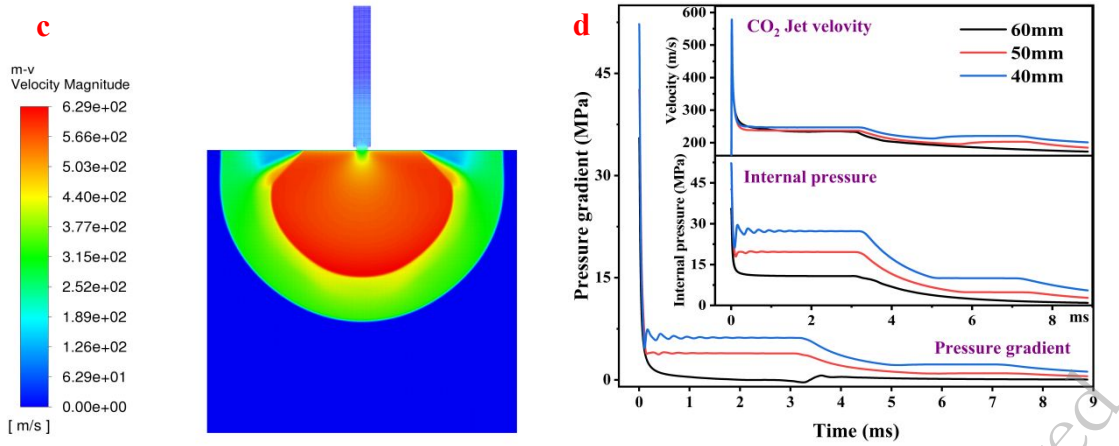


**Fig. 11.** | The velocity and pressure changes of $CO_2$ jet under different unloading orifice sizes. **a.** Nephogram of $CO_2$ rejection velocity under 60 mm unloading orifice size at 1 ms. **b.** Nephogram of $CO_2$ rejection velocity under 50 mm unloading orifice size at 1 ms. **c.** Nephogram of $CO_2$ rejection velocity under 40 mm unloading orifice size at 1 ms. **d.** The distribution discpline of 50 MPa $CO_2$ unloading flow field under different unloading orifice sizes.

As shown in Fig. 11, during the early 0.3 ms of the 50 MPa $CO_2$ unloading, the high-pressure $CO_2$ jet undergoes rapid expansion, leading to a sharp increase in jet velocity and a rapid drop in pressure. From 0.3 ms to 3 ms, the process enters a relatively stable phase, where the jet velocity remains nearly constant, and the gas pressure fluctuates within a narrow range. After 3 ms, both the jet pressure and velocity exhibit a unidirectional declining trend.

Throughout the jetting process, a smaller unloading orifice size results in a higher jet velocity, slower pressure decreases within the infiltration chamber, and a steeper pressure gradient between the chamber's interior and exterior. The accelerated $CO_2$ jet, carrying the ore, impacts the unloading head at a higher initial speed, creating more free surfaces that facilitate gas expansion within the ore. The $CO_2$ pressure inside the chamber decreases more gradually, slowing the reduction in gas pressure within the ore before it is exposed to the atmosphere. Additionally, a smaller unloading orifice increases the pressure loss of the $CO_2$ jet as it passes through the circular ring, establishing a pronounced pressure gradient that enhances ore pulverization.

Replacing rupture discs with mechanical valves to control high-speed gas unloading is a viable approach for achieving industrial-scale continuous production using the GRU method. This study demonstrates that appropriately adjusting the mechanical valve opening size can improve ore pulverization efficiency under consistent pressure conditions.

**4.2. Discussion about the scheme optimization**

While reducing the unloading orifice size can enhance ore pulverization, the feed size determines the optimal unloading orifice size. When the unloading orifice size is 40 mm, some BG iron ore becomes lodged in the discharge orifice without being pulverized. It is reasonable to speculate that further reducing the unloading orifice size to 30 mm or smaller could result in outlet clogging, completely obstructing ore pulverization. Determining the optimal unloading orifice size based on the characteristic size of the ore is an important research direction. Additionally, evaluating the energy consumption of GRU grinding compared to existing mechanical methods is crucial for assessing the feasibility of large-scale GRU production. Energy consumption analysis of GRU will also be a key focus of our subsequent research.

**Conclusion**

This study elucidates the influence of unloading orifice size on the ore pulverization by GRU. Laboratory experiments in both rear- mounted and front-mounted explosive setups indicate that reducing the orifice size increases the yield of fine particles and decreases overall particle size. When the unloading orifice size was reduced from 60 mm to 40 mm, the cumulative mass proportion of pulverized products smaller than 0.5 mm increased by 32% for LX iron ore and 40% for BG iron ore, respectively. The average particle size of the pulverized products for both ores also decreased significantly. Numerical simulations further indicate that smaller orifices during rapid unloading enhance the gas jet velocity, slow down the pressure drop inside the infiltration chamber, and increase the pressure loss as the $CO_2$ jet passes through the orifice. These conditions enhance the velocity and impact force of ore collisions with the discharge head, creating a higher internal-external pressure gradient upon ejection, thereby boosting ore pulverization. However, the experiment

results also show that excessively small orifices can cause blockages, hindering the pulverization process. Therefore, optimizing the orifice size relative to the feed size is crucial to maintaining efficient material ejection and effective ore pulverization. These insights provide valuable guidance for the industrial application of the GRU method and serve as a reference for designing future large-scale industrial equipment.

**Acknowledgements**

The authors wish to thank Luo Huan, Wang Qiuli and Liu Hanqing for their advice on experimental design. The authors also gratefully acknowledge the financial supports by the National Natural Science Foundation of China. [grant numbers 51934001].

**Declarations**

Conflict of interest the authors declare no competing interests.

**Reference**

[1] C.S. Philipp, S. Stefan, Sustainable supply chain management for minerals, Journal of Cleaner Production 151 (2017) 235-249.

[2] S.H. Ali, D. Giurco, N. Arndt, E. Nickless, G. Brown, A. Demetriades, R. Durrheim, M.A. Enriquez, J. Kinnaird, A. Littleboy, Mineral supply for sustainable development requires resource governance, Nature 543(7645) (2017) 367-372.

[3] M.C. Fuerstenau, K.N. Han, Principles of mineral processing, SME2003.

[4] J.-P. Duroudier, Size Reduction of Divided Solids, Elsevier2016.

[5] P. Agreement, Paris agreement, Report of the Conference of the Parties to the United Nations Framework Convention on Climate Change (21st Session, 2015: Paris). Retrived December, HeinOnline, 2015, p. 2017.

[6] Y.W. Yikai Liu, Qiusong Chen, Using cemented paste backfill to tackle the phosphogypsum stockpile in China: A down-to-earth technology with new vitalities in pollutant retention and $CO_2$ abatement, International Journal of Minerals, Metallurgy, and Materials 31(7) (2024) 1480-1499.

[7] T. Ou, J. Liu, W. Chen, Z. Ma, Y. Xiong, A novel IoT sensor and evolution model for grinding mill liner wear monitoring, Minerals Engineering 217 (2024) 108959.

[8] Y. Liu, G. Yan, R. Li, S. Xiao, M. Ren, L. Cheng, Multi-source unsupervised

domain adaptive mill load forecasting method based on deep learning and fusion features, Minerals Engineering 209 (2024) 108650.

[9] N. Matsanga, W. Nheta, N. Chimwani, A Review of the Grinding Media in Ball Mills for Mineral Processing, Minerals 13(11) (2023) 1373.

[10] V. Antonio, V. Alicia, Exergy of comminution and the Thanatia Earth's model, Energy 44(1) (2012) 1085-1093.

[11] J. Jack, S. Alex, Energy Consumption in Mining Comminution, Procedia CIRP 48 (2016) 140-145.

[12] D.W. Fuerstenau, A.Z.M. Abouzeid, The energy efficiency of ball milling in comminution, International Journal of Mineral Processing 67(1) (2002) 161-185.

[13] B.P. Numbi, J. Zhang, X. Xia, Optimal energy management for a jaw crushing process in deep mines, Energy 68 (2014) 337-348.

[14] J. Marcus, B. Magnus, E. Magnus, H. Erik, A fundamental model of an industrial-scale jaw crusher, Minerals Engineering 105 (2017) 69-78.

[15] A. Bahrami, M. Abdollahi, M. Mirmohammadi, F. Kazemi, A. Danesh, M. Shokrzadeh, A process mineralogy approach to study the efficiency of milling of molybdenite circuit processing, Scientific Reports 10(1) (2020) 21211.

[16] D. Jean-Paul, 3 - Ball and Rod Mills, (2016) 73-97.

[17] S.Y. Andre, T. Alex, A.M.E. Thiago, A review of modeling and control strategies for cone crushers in the mineral processing and quarrying industries, Minerals Engineering 170 (2021) 107036.

[18] W.C. Paul, D.M. Rob, Geometric analysis of cone crusher liner shape: Geometric measures, methods for their calculation and linkage to crusher behaviour, Minerals Engineering 160 (2021) 106701.

[19] P. Gao, W. Zhou, Y. Han, Y. Li, W. Ren, Enhancing the capacity of large-scale ball mill through process and equipment optimization: An industrial test verification, Advanced Powder Technology 31(5) (2020) 2079-2091.

[20] L. Maregedze, R. MASIKE, T. KANYOWA, K. CHITEKA, BALL MILL ENERGY EFFICIENCY OPTIMIZATION TECHNIQUES: A REVIEW, i-manager's Journal on Mechanical Engineering 13(4) (2023).

[21] L. Li, B. Wei, Q. Zhang, J. Zhang, X. Zhang, C. Wang, N. Li, Z. Liu, Evaluating the performance of an industrial-scale high pressure grinding rolls (HPGR)-tower mill comminution circuit, Minerals Engineering 191 (2023) 107973.

[22] C. Zhang, Y. Zou, D. Gou, A. Yu, R. Yang, Experimental and numerical investigation of particle size and particle strength reduction in high pressure grinding rolls, Powder Technology 410 (2022) 117892.

[23] C. Cooper, P. Wang, J. Zhang, R.X. Gao, T. Roney, I. Ragai, D. Shaffer, Convolutional neural network-based tool condition monitoring in vertical milling operations using acoustic signals, Procedia Manufacturing 49 (2020) 105-111.

[24] C.T. Jayasundara, R. Yang, A. Yu, Effect of the size of media on grinding performance in stirred mills, Minerals Engineering 33 (2012) 66-71.

[25] L. Taylor, D. Skuse, S. Blackburn, R. Greenwood, Stirred media mills in the mining industry: Material grindability, energy-size relationships, and operating conditions, Powder technology 369 (2020) 1-16.

[26] M. Can, O. Altun, Performance Comparison of the Vertical and Horizontal Oriented Stirred Mill: Pilot Scale IsaMill vs. Full-Scale HIGMill, Minerals 13(3) (2023) 315.

[27] K.R. Rajaonarivony, C. Mayer-Laigle, B. Piriou, X. Rouau, Comparative comminution efficiencies of rotary, stirred and vibrating ball-mills for the production of ultrafine biomass powders, Energy 227 (2021) 120508.

[28] H. Wei, C. Yumeng, The application of high voltage pulses in the mineral processing industry - A review, Powder Technology 393 (2021) 116-130.

[29] U. Andres, R. Bialecki, Liberation of mineral constituents by high-voltage pulses, Powder Technology 48(3) (1986) 269-277.

[30] P. Gao, Y.H. Qin, Y.X. Han, Y.J. Li, S.-Y. Liu, Strengthening leaching effect of Carlin-type gold via high-voltage pulsed discharge pretreatment, International Journal of Minerals, Metallurgy and Materials 28 (2021).

[31] G. Zhaolong, Z. Hongwei, Z. Zhe, C. Shirong, Z. Di, L. Xiangjie, T. Chao, Experimental study on the characteristics and mechanism of high-pressure water jet fracturing in high-temperature hard rocks, Energy 270 (2023) 126848.

[32] Y. Natarajan, P.K. Murugesan, M. Mohan, S.A.L.A. Khan, Abrasive Water Jet Machining process: A state of art of review, Journal of Manufacturing Processes 49 (2020) 271-322.

[33] A.J. Swart, P. Mendonidis, Evaluating the effect of radio-frequency pre-treatment on granite rock samples for comminution purposes, International Journal of Mineral Processing 120 (2013) 1-7.

[34] A.J. Buttress, J.M. Rodriguez, A. Ure, R.S. Ferrari, C. Dodds, S.W. Kingman, Production of high purity silica by microfluidic-inclusion fracture using microwave pre-treatment, Minerals Engineering 131 (2019) 407-419.

[35] Y.B. Fan, W.J. Duan, S.H. Li, J.Y. Qiao, Experiment on micron-sized particle production of iron ore by rapid unloading of liquid CO2, Powder Technology 327 (2018) 449-455.

[36] Y.B. Fan, J.Y. Qiao, S.H. Li, C. Feng, Micron-sized silicon carbide particle production via rapid unloading of high-pressure liquid CO 2, Journal of the Australian Ceramic Society 55(2) (2019) 595-600.

[37] M. Hesse, P. Asetre, R. Anderson, C. Edwards, C. Lee, O. Malpica, B. Klein, Experimental demonstration of comminution with transcritical carbon dioxide cycles, Powder Technology 407 (2022) 117615.

[38] F. Yongbo, F. Chun, L. Shihai, C. Li, Z. Li, Z. Genghao, H. Xingping, Production of Micron-Sized Particles of Bauxite by Circulating Pulverization Experiment, Advances in Materials Science and Engineering 2022(1) (2022) 6889003.

[39] S. Klaus, Breakage of spheres and circular discs, Powder Technology 143-144 (2004) 2-18.

[40] Q. Yin, F. Wen, Z. Tao, H. Pu, T. Deng, Y. Meng, Q. Meng, H. Jing, B. Meng, J. Wu, Effects of aggregate size distribution and carbon nanotubes on the mechanical properties of cemented gangue backfill samples under true triaxial compression, International Journal of Minerals, Metallurgy and Materials 32(2) (2025) 311-324.

[41] Z. Genghao, F. Yongbo, Y. Renshu, L. Shihai, Influence of ore size on the production of micro-sized ore particles by high-pressure gas rapid unloading, Powder

Technology 427 (2023) 118716.

[42] The Rosin-Rammler particle size distribution, Resource Recovery and Conservation 5(3) (1980) 275-277.

[43] K. Raj, R.G. Srikanth, K.J. Arun, M.P. Chetan, Study of the discharge behavior of Rosin-Rammler particle-size distributions from hopper by discrete element method: A systematic analysis of mass flow rate, segregation and velocity profiles, Powder Technology 360 (2020) 818-834.

[44] H.Y. Cheng, S.C. Wu, X.Q. Zhang, A.X. Wu, Effect of particle gradation characteristics on yield stress of cemented paste backfill, International Journal of Minerals, Metallurgy and Materials 27(1) (2020) 10-17.